Proceedings of the 2012 3rd ASME Micro/Nanoscale Heat & Mass Transfer International Conference
MNHMT1012
March 3-6, 2012, Atlanta, Georgia, USA

MNHMT2012-75174

NANO FILTRATION AND SENSING OF AMINOGLYCOSIDES USING WHISPERING-GALLERY MODE RESONATORS

Lei Huang
Department of Mechanical and Aerospace Engineering, Rutgers University, Piscataway, NJ 08854, USA

Zhixiong Guo
Department of Mechanical and Aerospace Engineering, Rutgers University, Piscataway, NJ 08854, USA
guo@jove.rutgers.edu

ABSTRACT

For the first time optical WGM micro resonator embedded in a microelectrofluidic system with integrated functions in sensing and nano filtration was proposed. Aminoglycosides were considered as the analyte molecules. The filtration process and analyte concentration were traced by measuring the WGM resonance frequency shift. A correlation between the frequency shift, and the analyte feed concentration and the applied voltage gradient was obtained, which reveals a linear relationship between the resonance frequency shift and the analyte concentration and an exponential growth with the applied voltage gradient. The applied voltage gradient influences the filtration capability through its effect on adsorption and desorption processes. The second-order WGM was found to be able to provide a higher sensitivity as compared with the first-order. The WGM sensor was found to function at pico Molar concentration.

INTRODUCTION

Nanofiltration [1] which is widely used in many industrial sectors offers several advantages such as low operation pressure, high flux, high retention of multivalent anion salts and an organic molecular above 300 *Da*. In addition to the capability to reduce the ionic strength of the solution, nanofiltration membranes can remove hardness ions, organics and particulate contaminants. As such, nanofiltration has drawn much attention in recent decades in the field of water treatments [2, 3], food industry [4], pretreatment for desalination [5], textile industry [6], and separation for biological or biochemical analysis [7]. The transport through nanofiltration membranes is extremely complicated and numerous models have been developed to describe the process [8-10]. Most widely-adopted models for describing ion and neutral solute retention with nanofiltration are derived from the space charge model [11-14]. In the scope of this theory, the so-called Donnan steric partitioning pore model (DSPM) [11, 12], which is based on the extended Nernst-Planck equation, was successfully used to describe the transport through the nanofiltration membranes [15].

There is an increasing awareness of micro-opto-fluidic systems (MOFS), which employ hybrid optical and microfluidic technologies in a micro environment to perform novel functionality and in-depth analysis [16-21]. MOFS can be realized via a simply-integrated chip solution, combining fluid flow and optical sensor in a single microchannel, in which the fluid acts as a medium which carries analytes such as biomolecules and chemicals in the microchannel for optical detection. In 1999, Guo *et al*. [17] proposed a rapid yet accurate optical interferometric method for measuring mass diffusion coefficients in microchannels with aqueous solutions within 100 sec. In 2005, Leung *et al*. [18] developed a continuous flow microfluidic reactor, using a confocal Raman microscopy detector for online monitoring, and significantly reduced measurement time from 48 h to only 10 min. Cui *et al.* [19] has recently implemented an on-chip optofluidic microscopic system using the surface plasmon resonance technique to measure living C. *elegans* within 0.5 sec. Burg *et al*. [20] has demonstrated a suspended microchannel resonator with embedded microfluidic channels for ultralow volume universal detection. As compared with conventional measurement instrument, the sample quantity in a microfluidic channel is substantially reduced. Traditionally, pressure is used in these devices to induce controllable fluid flow in microchannels. However, incorporation of a pressure pump or valve into a microchannel is challenging and restrictive in many situations. Thus, other manipulation schemes such as use of applied electric voltage [21] may be needed, leading to combined micro-opto-electro-fluidic systems (MOEFS).

Nowadays, research on whispering-gallery mode (WGM) based biosensing has attracted increasing attention, because of its extremely high sensitivity in the detection of molecules or nano-entities [22-25]. At a resonance, photons are trapped and

internally reflected in an orbit within the resonator surface of circular shape. The resonance induces a strong evanescent wave field in the surrounding. As the photons guided by total internal reflection in the resonator circulate many times, they interact repeatedly with adsorbate on the surface of the resonator, leading to resonance frequency shifts [22-24]. Less well known is that the binding of polarizable molecules to the surface of a light guide can interact with this evanescent wave and slightly increase the path length and number of wavelengths of light through the waveguide. In 2002, Arnold *et al.* [23]demonstrated a device in which each photon guided by total internal reflection in a silica sphere (radius of about 100 μm) is recirculated many times, thereby providing a mechanism for increasing sensitivity.

Aminoglycosides are a large class of antibiotics that are characterized by two or more amino sugars lined by glycosidic bonds to an aminocyclitol component. They exhibit activity against both Gram-negative and Gram-positive organisms. These antibiotics are highly potent broad-spectrum antibiotics with many desirable properties for the treatment of life-threatening infections for people and animals. They may be administered orally as feed additives or directly injected. However, the use of aminoglycosides may result in drug residues in food and livestock products, particularly if proper withdrawal times for treated animals have not been practiced [26], As such, to safeguard human health, there is a great need for improved analytical methods to confirm the presence of aminoglycoside residues in food or the edible tissues of livestock. In the present study, Neomycin, which is among the aminoglycosides, is taken as the sample analyte since it has a relatively large molar volume which would induce a higher refractive index change to the micro resonator. The sample molecular weight and refractive index are assumed as 614.64 *g/mol* and 1.674, respectively. Pure water at neutral pH is taken as solvent. Each neomycin molecule carries five effective surface charges [27].

In this work, a new concept platform that can simultaneously perform nanofiltration and optical sensing functionalities is proposed and investigated via the finite element method. An optical WGM micro device, which acts as a micro sensor as well as a nanofilter, is integrated with a microelectrofluidic channel to provide a new MOEFS platform for label-free detection. The analyte solution flow in the microchannel is driven by an external electric potential. The whole process is coupled by the charge transport equations, the Poisson equation, the conservation of momentum equation, the energy conservation equation and Maxwell's equations. All the governing equations are solved via the finite element method using commercial software COMSOL.

MATHEMATIC FORMULATION

Figure 1 shows the sketches of the considered MOEFS. The system consists of a microfluidic channel with two electrodes and an optical WGM resonator as the micro sensor which contains porous structure interior. A ground electrode can be embedded inside the dielectric resonator. Analyte solution and buffer solution are fed through the inlet port toward the outlet port. The solution with charged analyte completes an electric circuit between the high voltage anode and the ground electrode. As a result, the charged analytes are directed to the optical sensor through the electrostatic fluid flow, and transported into the porous structure inside the micro resonator. The WGM-based optical resonator coupled with a waveguide is integrated in a section of the microchannel. The enlarged view in Figure 1 provides a detailed sketch of the simulation region with both the analyte transport and the sensor in which h indicates the inner width of the channel, l is the length in the simulation domain, d indicates the resonator diameter, and w is the width of the waveguide. A laser beam is focused into the waveguide from which the light tunnels into the micro resonator.

The micro resonator (d = 10 μm) is made of silicon nitride with porous structure, the waveguide (w = 2 μm) is made of pure silicon nitride, and the embedded electrode inside the micro resonator is made of copper. The inner width of the channel was h = 11.2 μm; and the channel length in the simulation domain was l = 60 μm. The electrical potential gradient is measured from the anode to the ground embedded electrode inside the micro resonator. Single-mode laser with wavelength around 624 *nm* is used to trigger a WGM resonance inside the micro resonator through the waveguide. The gap between the micro resonator and waveguide is set at 600 *nm*. The extremely dilute analyte solution can be assumed to have the permittivity, viscosity, density and refractive index of pure water.

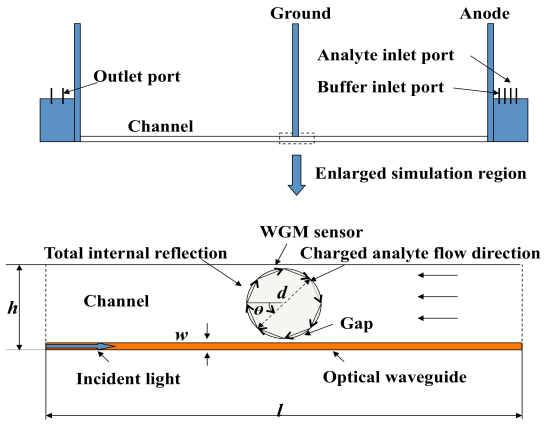

Fig. 1 Sketches of the MOEFS with a WGM sensor and the enlarged view of the simulation region.

The surface saturation concentration is taken based on the total available surface density of SiO^- sites on the pore walls. It should be pointed out that the surface saturation concentration is calculated on the assumption that the adsorption of hydroxide ions and hydronium ions onto the pore walls are negligible and does not significantly affect the adsorption capability of the surface to neomycin molecules. We select the neutral pH value as a study case. In a Si_3N_4/H_2O solution, the neutral SiOH species becomes the predominant one, whereas the SiO^- sites

increase [28]. It is known that the neomycin molecules carry positive charges at neutral pH value [27]. The adsorption and desorption coefficients of neomycin are assumed constant, close to the values given by the experiment of Yeung *et al* [29]. The property values used in the present simulation are summarized in table I.

Table I. Parameters used in this work (at 300K, neutral pH)

Symbol	Description	Value used
w_1	Mobility of neomycin in water	1.5×10^{-14} *mol·s/Kg*
w_2, w_3	Mobility of ions	5×10^{-13} *mol·s/Kg*[30]
D_1	Diffusivity of neomycin in water	3.26×10^{-10} m^2/s
D_2, D_3	Diffusivity of ions	5×10^{-9} m^2/s [31]
K_{ads}	Adsorption coefficient of neomycin	2.2 $m^3/(mol\cdot s)$
K_{des}	Desorption coefficient of neomycin	1×10^{-3} $/s$
Θ	Surface saturation concentration	8.3×10^{-7} mol/m^2
ε_f	Permittivity of water	6.93×10^{-10} $C/(V\cdot m)$
ε	Permittivity of silicon nitride	3.54×10^{-11} $C/(V\cdot m)$
F	Faraday constant	9.65×10^{4} C/mol
ρ	Density of water	1.0×10^{3} Kg/m^3
υ	Viscosity of water	1.0×10^{-6} m^2/s
n_m	Refractive index of bulk silicon nitride	2.01
n_s	Refractive index of water	1.33
n_A	Refractive index of neomycin	1.674

A. Governing equations

The present work applies the volume-average technique [10] to the fundamental equations in the porous region. We start from the charge transport equations. To simplify the computation, the electro hydrodynamic system only consists of three species ions, the positive hydronium ions, the negative hydroxide ions and the analyte charged species. As such, the charge transport for analyte dissolving in pure water includes aminoglycoside analyte, the positively-charged ions and negatively-charged ions [32]. The transport equations are:

$$\frac{\partial C_i}{\partial t} + K_{i,c}\vec{V}\cdot\nabla C_i = \nabla\cdot(z_i w_i F C_i \nabla\Phi) + K_{i,d} D_i \nabla^2 C_i, \quad i = 1,2,3 \qquad (1)$$

where C is molar concentration; z is the valence number (in this work, we assume z1=5, z2= -z3= 1); w is the mobility under an external electric potential; Φ is the electric potential; D is the diffusion coefficient; and F is the Faraday constant. Subscripts i= 1, 2, and 3 indicate the analyte, hydroxide ion and hydronium ion, respectively. Superscript m indicates the micro resonator. Solutes are drawn by convection, diffusion, and electrical forces resulting in a solute flux through the resonator, which acted like a nanoporous membrane in the study. The porous structure was considered to consist of a parallel association of identical straight cylindrical pores. The solution was sufficiently diluted so that both electrical potential and ion concentrations can be considered as radially constant. Inside the resonator, due to the existence of nano-structured pores, a modified transport equation should be employed which differs from the regular Nernst-Planck equation on the use of drag coefficients for convection $K_{i,c}$, and diffusion $K_{i,d}$. Such coefficients are necessary to correct the convective and diffusive transport in the bulk solution for a solute confined in a pore. In bulk solution, both drag coefficients can be simply adopted as unit, while in porous medium, they can be expressed as [15]:

$$\lambda_i = \frac{r_i}{r_p}, \phi_i = (1-\lambda_i)^2, \ i = 1,2,3 \qquad (2)$$

$$K_{i,c} = K_c(\lambda_i) = (2-\phi_i)(1 + 0.054\lambda_i - 0.988\lambda_i^2 + 0.441\lambda_i^3), \ i = 1,2,3 \qquad (3)$$

$$K_{i,d} = K_d(\lambda_i) = 1 - 2.3\lambda_i + 1.154\lambda_i^2 + 0.224\lambda_i^3, \ i = 1,2,3 \qquad (4)$$

Here r_i and r_p represent the hydrodynamic solute radius and the effective pore radius, respectively; Subscripts i= 1, 2, and 3 indicate the analyte, hydroxide ion and hydronium ion, respectively.

As the electric potential field is irrotational, it can be conveniently expressed by the following Poisson equation in bulk solution:

$$\varepsilon_f \nabla^2 \Phi = -\tau\rho_E \qquad (5)$$

where

$$\rho_E = F\left(\sum_{i=1}^{3} z_i C_i\right) \qquad (6)$$

Here, ρ_E is the total charge density, ε_f is the permittivity of fluid, and τ is the tortuosity, defined by $\tau=(l/L)^2$, l is the average length of travel for flow along the pore path and L is the physical length of the porous structure. In the Poisson formulation, the permittivity of the solution is assumed uniform. The conductivity field is dominated by charges densities and charges' mobility is assumed constant.

Under the effect of an external electrical field, a modified Navier-Stokes equation[33] can be adopted to describe the equation of conservation of momentum for the incompressible aqueous solution:

$$\frac{\partial\vec{V}}{\partial t} + \frac{\vec{V}}{\tau}\cdot\nabla\frac{\vec{V}}{\tau} = -\frac{\nabla(P)}{\tau\rho} + \frac{\upsilon}{\tau}\nabla^2\vec{V} - \frac{\rho_E}{\tau\rho}\nabla\Phi + \frac{\xi\Gamma}{\tau} \qquad (7)$$

where ρ is the liquid density, $\vec{V}$ is the volume-average velocity, P is the pressure, and υ is the dynamic viscosity. The electric potential is coupled to the momentum equation via the

addition of the electric force term. ξ is the porosity of the medium (ξ =1 in the bulk solution region), $\rho_E \nabla\Phi / \tau\rho$ represents the electrical driving force due to the net volume charge inside the porous medium; The force term is caused by the micropore structure and thus can be defined as $\xi\Gamma / \tau$, indicating the linear superposition of Darcy term and Forchheimer term, based on Ergun's empirical relation and [33]:

$$\Gamma = -\frac{\upsilon \vec{V}}{K} - \frac{F_\varepsilon \left|\vec{V}\right| \vec{V}}{\sqrt{K}} \tag{8}$$

where K and F_ε is the permeability of the porous medium and the geometric function, respectively. The F_ε can be written as [33]:

$$F_\varepsilon = \frac{1.75}{\sqrt{36 k_0 \xi^3 \sqrt{\tau}}} \tag{9}$$

And noting the model for the porous medium is parallel cylinder tubes, the permeability can be described as [33]:

$$K = \frac{\xi^3 d^2}{36 k_0 (1-\xi^2)\sqrt{\tau}} \tag{10}$$

where k_0 is the Kozeny constant and in most cases is found to be 2 [33]. In the present study, the tortuosity is assumed as 1. It is worth mentioning that in the bulk fluid region, due to the format of permeability, the added force term $\xi\Gamma / \tau$ in Eq. (7) vanishes.

The micro resonator and waveguide are made of a dielectric material. In the optical device, the EM wave and photon tunneling can be described by time-dependent Maxwell's equations [34] as follows:

$$\nabla \cdot \vec{E} = \frac{\rho_E}{\varepsilon}, \ \nabla \times \vec{E} = -\mu \frac{\partial \vec{H}}{\partial t}, \tag{11}$$

$$\nabla \cdot \vec{H} = 0, \ \nabla \times \vec{H} = J + \varepsilon \frac{\partial \vec{E}}{\partial t}, \tag{12}$$

where $\vec{E}$ and $\vec{H}$ are the electric and magnetic field vectors, respectively; μ and J are permeability and total current density, respectively; and ε is the permittivity. For time-harmonic waves, $E(r,t)=E(r)exp(i\omega t)$ and ω is the angular frequency, Maxwell's equations are then simplified to the Helmholtz equations as follows:

$$\nabla^2 \vec{E} + \mu\omega^2 \varepsilon \vec{E} = 0, \tag{13}$$

$$\nabla^2 \vec{H} + \mu\omega^2 \varepsilon \vec{H} = 0. \tag{14}$$

Under WGM resonances, the EM field in a 2-D micro resonator typically consists of equatorial brilliant rings. The rings are located on the same plane as the waveguide [22]. Consider in-plane transverse electric (TE) waves, the EM fields can be simplified as:

$$\vec{E}(x,y,t) = \vec{E_z}(x,y)\vec{e_z}e^{i\omega t}, \tag{15}$$

$$\vec{H}(x,y,t) = [\overrightarrow{H_x}(x,y)\vec{e_x} + \overrightarrow{H_y}(x,y)\vec{e_y}]e^{i\omega t}. \tag{16}$$

B. Initial and Boundary conditions

In the present simulations, neutral velocity boundary conditions which act like there were no boundaries are assumed in the streamwise direction. The whole system is considered at a constant temperature 300 *K*. For the charged species, convective flux and constant concentration (feed concentration) are adopted at the outlet and inlet of the flow, respectively. Initially there is no analyte distributed in both the bulk solution and the porous regions. The solution is initially stationary. Non-slip conditions on the walls are assumed. The following boundary conditions are employed on the physical walls:

$$\nabla\Phi \cdot \vec{n} = 0 \tag{17}$$

$$\nabla C_i \cdot \vec{n} = 0, \quad i = 1,2,3 \tag{18}$$

$$\vec{V} \cdot \vec{n} = 0, \ \vec{V} \cdot \vec{t} = 0 \tag{19}$$

where $\vec{t}$ and $\vec{n}$ are the tangential and normal vectors of the wall, respectively. Equations (17) and (18) are respectively the condition that the boundary is nonconductive and that there is no ion diffusion across the walls. Equation (19) is the condition that the walls are not penetrative.

At the interface between the micro resonator and bulk solution, a continuity condition is adopted to the ions concentrations.

The bio-molecule adsorption on a solid surface is involved in a wide range of phenomena and applications and represents a complicated field of biomaterials which has been studied for decades. Physical adsorption at a liquid-solid interface is due to favorable van der Waals, ionic and polar interactions. Due to a net charge and a permanent dipole, most molecules align and migrate in an electric field. On a hydrophilic surface, the electrostatic attraction between oppositely charged material is often the major driving force for adsorption of bio molecules [35]. Silicon nitride (Si_3N_4) is selected as the sensor material for waveguide and microdisk. Langmuir approach [36] is adopted to describe the molecule adsorption process. The key assumptions are: (a) only a monolayer forms by adsorption; (b) the adsorbing surface is composed of discrete, identical, and non-interacting sites; (c) the adsorption process for each molecule is independent; and (d) there is no molecule-molecule interactions since the concentration is very low.

Due to the extremely complex geometry inside a nano porous structured medium, the effective adsorption surface technique is adopted to the adsorption of aminoglycoside onto pore walls. The main concept is illustrated in Figure 2 in which

three virtual adsorption surfaces together with the embedded electrode surface are proposed as four effective adsorbing interfaces. Each interface area is proportional to the total surface area of the pore walls inside each ring region and the proportionality is a constant A, i.e.,

$$\frac{\xi \times (R_{i-1}^{\ 2} - R_i^{\ 2})}{r} = AR_i,\ i = 1,2,3,4 \qquad (20)$$
$$\text{let} R_0 = R$$

where the resonator is considered with a radius of R=5μm and a porosity of 0.28; the embedded electrode is set to have a radius of R_e=4μm; r =20nm is the radius of pores inside the resonator; R_i represent the radius of rings following an order from the embedded electrode to the micro resonator outer surface. It is worth mentioning that the surface area factor A is assumed to be a constant for all virtual rings shown in the plot. Applying Eq. (20) to five virtual ring surfaces, the surface area factor A can be calculated as 7.287, and radius are calculated as 4.249μm, 4.499μm, and 4.749μm, respectively.

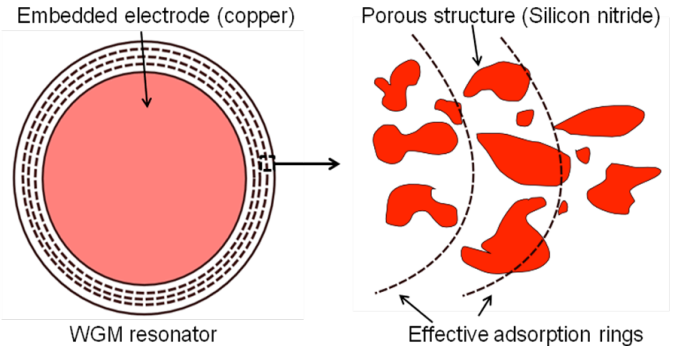

Fig. 2 Sketches of the WGM resonator with a porous structure and an enlarged view of effective adsorption rings.

Now we are ready to consider boundary conditions for charge transport equations. Assuming there is no surface diffusion on pore walls, the boundary conditions with respect to C_i are prescribed as:

$$\vec{n} \cdot (-D_1 K_{1,d} \nabla(C_1) + z_1 w_1 F(C_1) \nabla\Phi + (C_1) K_{1,c} \vec{V}) = -K_{ads}(\frac{C_1}{\xi})(\Theta - C_s) + K_{des} C_s, \qquad (21)$$

$$\nabla(C_1) \cdot \vec{n} = 0, \quad i = 2,3 \qquad (22)$$

Here, K_{ads} and K_{des} are the adsorption coefficient and desorption coefficient, respectively. Θ indicates the surface saturation density value depending on the available surface adsorption sites density on pore walls. The surface density of adsorbate, C_s, is governed by:

$$\frac{\partial C_s}{\partial t} = K_{ads}(\frac{C_1}{\xi})(\Theta - C_s) - K_{des} C_s \qquad (23)$$

It is worth mentioning that the adsorption and desorption processes only occur at the pore walls and the nanoporous structure is assumed not to significantly affect the adsorption and desorption behavior.

As to the boundaries of the calculation domain for Maxwell's equations, the low-reflecting boundary condition, which indicates that only a small part of the EM wave is reflected and the wave propagates through the boundary almost as if it were not present, is adopted [24]:

$$\vec{e}_z \cdot \vec{n} \times \sqrt{\mu}\vec{H} + \sqrt{\varepsilon}\vec{E}_z = 0 \qquad (24)$$

The light source term $\overline{E_{0z}}$, which propagates inwards through the entry of the waveguide, can be treated as an electrically low-reflecting boundary expressed by:

$$\overrightarrow{E_{0z}} = \frac{1}{2\sqrt{\varepsilon}}(\vec{e}_z \cdot \vec{n} \times \sqrt{\mu}\vec{H} + \sqrt{\varepsilon}\vec{E}_z) \qquad (25)$$

In present computations, the light source term is assumed to be uniform and unity at the entry of the waveguide.

RESULTS AND DISCUSSION

In 2011, Huang and Guo [37] validated the adsorption of bovine serum albumin (BSA) at two different concentrations (20 pM and 500 pM) onto a silica micro resonator at pH 6.6 in the absence of external electrical field through comparison with the experimental results by Yeung *et al* [29, 38]. As discussed in that work, both the experimental and calculated results exhibit Langmuir-like adsorption kinetics, and the simulations agreed well with the experimental measurements, indicating the feasibility of using the present model to simulate the adsorption and desorption process.

In the bulk solution at neutral pH value, the hydroxide ions and hydronium ions are in equilibrium and the ion concentration is assumed 100 nM each at room temperature. Samples are driven to move once the external electrical potential difference is applied to the MOEFS. As a result, some of them will be transported through the porous structured resonator and adsorbed at the pore walls till the whole system reaches a new equilibrium. A typical analyte concentration distribution and a representative resonance electric field are shown in Figures 3 (a), (b) and (c), respectively. In the simulation, the applied voltage gradient is 17.7 V/cm (calculated by taking an effective working distance from the surface of the embedded ground electrode to the anode electrode) and the neomycin bulk concentration is 10 pM. Figure 3 (a) illuminates the steady-state distribution of the neomycin analyte concentration in both bulk solution and the micro resonator, and the equipotential lines of the electrical potential field. It is seen that most of the positively-charged analytes accumulate inside the micro resonator indicating the micro resonator itself working as a filter with nano pores. Furthermore, the vicinity around the embedded electrode surface is the most concentrated region, which justifies the fact

that in such a system, the applied electrical potential is a predominant driven mechanism over the convection and diffusion for charged analyte transport. As a result, the analyte concentration inside the micro resonator is substantially enriched, especially in the region around the embedded electrode, with maximum concentration about 10 times of the feed concentration. The adsorption of neomycin molecules into the micro resonator varies the WGM resonance frequency by inducing an effective refractive index change. It's worth mentioning that in a fluid composed of electrically charged molecules and ions, each pair of particles interact through the Coulomb force which complicates the theoretical treatment of the fluid. In the present study, conditions in which the extremely dilute solution is treated and an external electrical field is applied leading to a reasonable assumption that the screening effect could be ignored. Figure 3 (b) displays the distribution of the time-varying harmonic electric field in a small region ($20\times13.5\ \mu m^2$) around the sensor under a first-order WGM resonance. It is clearly seen that most of the energy is well confined inside the micro resonator under the first order of WGM resonance. The resonance frequency is shifted from a base frequency 262.355596 *THz* for the case without analyte adsorption to 262.355054 *THz* for the case an effective refractive change induced by the adsorption of neomycin molecules at steady state. Figure 3 (c) demonstrates the second mode of WGM in which the resonance frequency shifts from a base frequency 265.874573 *THz* to 265.873777 *THz* under the same condition. It can be seen that the second WGM resonance possesses less energy but offers higher shift as compared with the first mode. The analyte adsorption inside the porous structured micro resonator does not obviously degrade the resonance quality and the Q-factor remains in the order of 10^6.

An investigation regarding the applied voltage gradient effect on the bulk concentration is further carried out. The bulk concentration along the radial direction of the micro resonator is illustrated in Figure 4. Simulations are taken for the case of a feed concentration of 10 *pM* with different applied voltage gradients. The plot demonstrates that higher applied voltage gradient leads to more analytes accumulated in the vicinity of the embedded electrode, as well as the pores interior of the micro resonator. As the applied voltage gradient increases, the bulk concentration and its gradient inside the micro resonator also increase as a result of a stronger driven mechanism over the convection and diffusion.

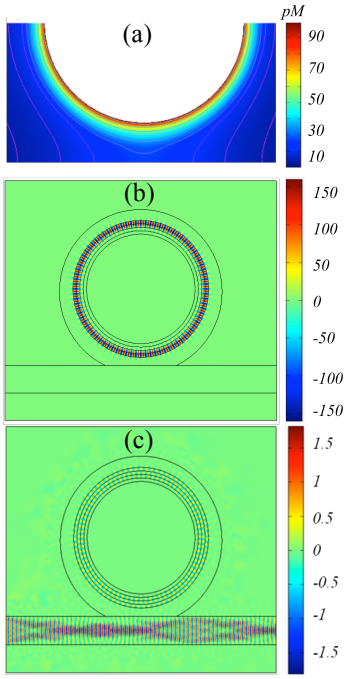

Fig. 3 Representative analyte concentration field (a), WGM resonance electric field under the first mode (b) and under the second mode (c).

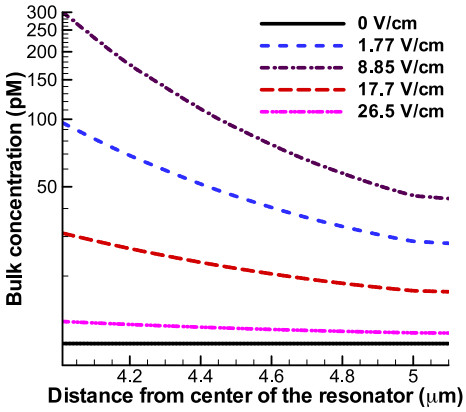

Fig. 4 The bulk concentration distribution along the radial direction with a feed concentration of 10 *pM* for different applied voltage gradients.

To further inspect the influence of the applied voltage, the variations of the averaged analyte surface density at equilibrium versus the applied voltage gradient for two different feed concentrations (10 *pM* and 50 *pM*) are plotted in Figure 5. It is worth mentioning that the surface density shown in the plot was averaged from the effective adsorbing rings plotted in Figure 2. It is seen that the analyte surface density monotonously increase as the applied voltage gradient increase up to 26.5 *V/cm* indicating higher voltage gradient is favored to introduce more adsorbed analyte into the micro resonator. Moreover, a higher feed concentration is also attributable to higher absorbed analyte surface density.

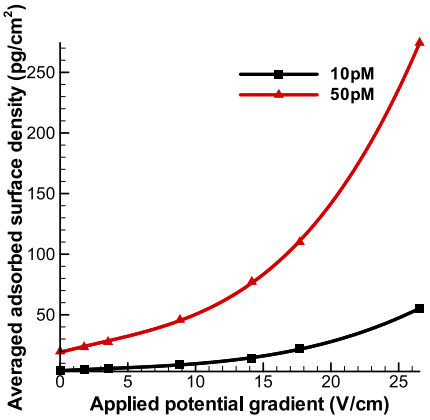

Fig. 5 The averaged surface density versus different applied voltage gradients.

In addition to the effect of applied voltage gradient on the adsorbed analyte surface density, the feed concentration set at the inlet also contributes to the adsorbed amount of analytes into the porous medium. Figure 6 illustrates a linear relationship between the feed concentration and the adsorbed analyte surface density, which is well expected since the analyte bulk concentration is linearly proportional to the feed concentration. Consistently, the picture indicates that higher applied voltage gradient is more favored to obtain more adsorbed analyte into the micro resonator.

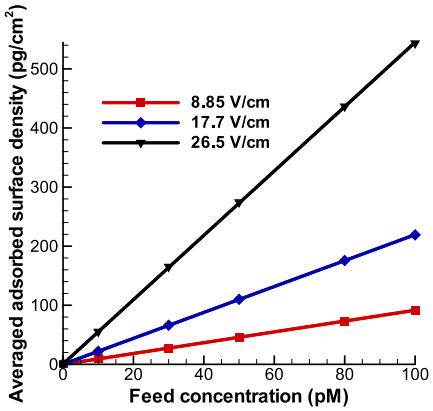

Fig. 6 Influence of feed concentration on adsorbed surface density.

The analyte adsorption onto a solid surface is a time-dependent process. Figure 7 demonstrates the time evolution of the averaged surface density of the adsorbed analyte versus the applied voltage gradient. Cases 10 *pM* and 50 *pM* with an applied voltage gradient 17.7 *V/cm* and 10 *pM* with a 26.5 *V/cm* applied voltage gradient are investigated. In general, the adsorption of bio-molecules onto a solid/liquid interface can be described through two distinct kinetic regimes [36], the transport-limited and adsorption-limited regimes. In this study, the positively-charged analyte moved toward the lower electrical potential under the external electrical effect. Once reach the micro resonator surface, the analytes then transport through the porous medium toward the embedded electrode with drag effects induced by the nano pores inside the micro resonator. Both of the motions mentioned are transport-limited mechanism. During the transport inside the micro resonator, the adsorption and desorption processes happen at the pore walls. As the adsorption and desorption processes proceed, according to the monolayer assumption, surface active sites diminish, and thus, reducing the rate of adsorption and the deposition process. It is said in the adsorption-limit regime in the vicinity around the pore walls. The adsorption and desorption processes are then balanced when a significant fraction of the surface is covered, indicating the saturation was achieved. The results in Figure 7 show Langmuir-like adsorption kinetics, following the formula $C_{s=}\ C_{sat}[1\text{-}exp(\text{-}t/\tau)]$, in which C_{sat} is the absorbate surface density at saturation and τ is the time constant. The time constants for the cases of 10 *pM* and 50 *pM* with a same applied voltage gradient 17.7 *V/cm* and the case of 10 *pM* with a 26.5 *V/cm* applied voltage gradient are obtained as 18.39, 16.64 and 44.34 hrs, respectively, through best fitting. It should be noted that the higher applied voltage gradient significantly increases the time constant. It is believed to result from a stronger competition between the adsorption and convection at higher applied voltage gradient. This competition limits the system in the transport-limited regime, thereby, increasing the time constant. It can be clearly seen that in Figure 7, the cases with the lower applied voltage gradient, 17.7 *V/cm*, are located in the adsorption-limited regime and the case with an applied voltage gradient of 26.5 *V/cm* locates in the transportation-limited regime.

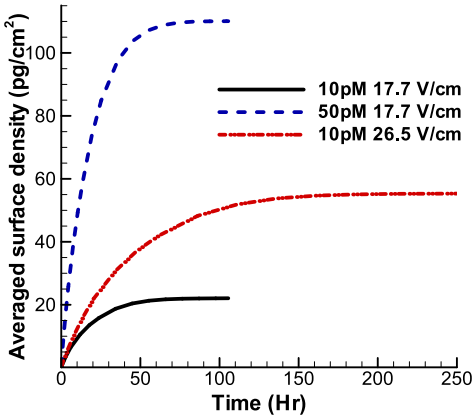

Fig. 7 The time trace of the adsorbed analyte on the micro resonator surface for three different cases.

In applications utilizing the interaction between the evanescent field and the external conditions change (i.e. refractive index change, molecules adsorption, etc.), the fundamental mode (i.e. the first order of WGM) which only has one intensity peak is always favored. This is because the fundamental mode is featured by processing only one intensity peak in both radial and polar directions of the micro resonator and the field maximum is the closest to the equator surface. However, differing from the sensing mechanism utilizing the interaction of the WGM and the external effective change, the dominant effect in the present study is introduced through the

adsorption of the analyte into the micro resonator. In a porous structured micro resonator, the effective index can be approximately expressed as the following in the absence of analytes adsorption:

$$n_m = (1-\xi)\times n_{Si_3N_4} + \xi \times n_{solution}$$
$$n_{solution} = n_{water} + C^m \times molar\ volume \times n_A \quad (26)$$

where ξ is the porosity; n_m is the effective refractive index of the porous structured micro resonator; $n_{solution}$ represents the refractive index confined inside the nano pores; n_{water} and n_A indicate the refractive indices of pure water and neomycin, respectively; *molar volume* is the volume occupied by the analyte molecules in the solute. As such, the effective index change induced by the adsorption of analytes can be expressed as:

$$\Delta n_m = \xi_1 \times n_A + (\xi - \xi_1)\times molar\ volume \times n_A \times \Delta C^m \approx \xi_1 \times n_A \quad (27)$$

ξ_1 represents the total volume occupied by the adsorbed analyte molecules on pore walls.

Figure 8 illustrates the fundamental and the second orders of the WGM propagating inside the micro resonator shown in Figure 3. A bulk concentration along the radial direction is also demonstrated for the case of 17.7 *V/cm* applied voltage gradient and 10 *pM* feed concentration. The second order of radial mode possesses two intensity peaks along the radial direction while the fundamental mode only has one peak. According to the plot, most of the analytes accumulate around the vicinity of the embedded electrode and then the bulk concentration gradually decreases toward the resonator surface. It can be seen that the second order of WGM overlaps more with the bulk concentration distribution than the first order of WGM does, indicating more energy of the propagating WGM interacts with the effective refractive index change of the micro resonator. It is calculated that fractions of energy of propagating WGM in the porous regions are 0.075%, 3.34%, 35.6% and 60.9% for the first order and 5.3%, 41.0%, 30.0% and 23.3% for the second order, following an order from the embedded electrode to the microresonator surface. The greater fraction of energy overlapping with the bulk concentration distribution leads to a stronger interaction between the WGM and the effective refractive index change inside the micro resonator. As such, higher sensitivity can be provided through tracking the second order of WGM.

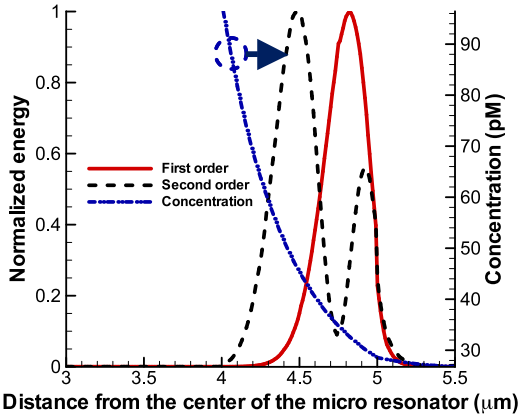

Fig. 8 The normalized energy distributions for the first and second order of radial mode and the overlap with the concentration distribution for case 17.7 *V/cm*, 10 *pM*.

The time evolutions of the frequency down shift induced by the analyte adsorption into the micro resonator surface at neutral pH value are investigated and shown in Figure 9. The frequency down shift curve reflects the detection of a real WGM sensor employing a certain order of WGM. Two different cases are studied. The applied voltage gradients are set to be 17.7 and 26.5 *V/cm* with corresponding analyte feed concentrations of 50 and 10 *pM*, respectively. Via the Langmuir fitting, the time constants for the case of 17.7 *V/cm* and 50 *pM* are found to be 18.31 and 17.44 hrs, for the first order and second order modes, respectively. Similarly, the time constants are found to be 40.72 and 34.06 hr for the case of 26.5 *V/cm* and 10 *pM*, under the first order and the second order resonance, respectively. The small difference between the time constants via best fitting of time evolutions of the adsorbed analyte surface density and the WGM frequency down shift verifies that the time trace of the filtration process via adsorption onto pore walls can be accurately monitored by the detection of the WGM frequency shift.

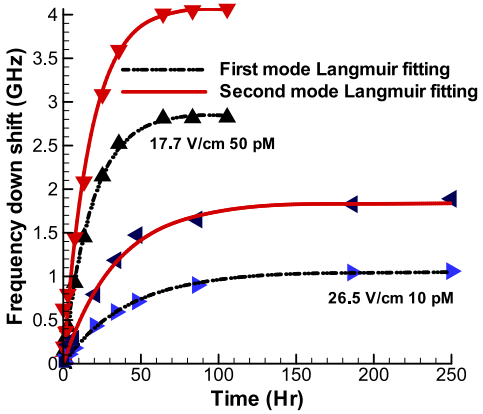

Fig. 9 The time evolution of WGM frequency down shift and Langmuir fitting for cases 17.7 *V/cm* 10 *pM* and 26.5 *V/cm* 50 *pM* under the first and second resonance modes.

Figure 10 shows the relationship between the detected frequency down shift and the analyte concentration at steady state in the solution with a neutral pH value. Both the sensor curves detected by the first order and the second order of WGM are displayed in the figure. It is seen that the shift increases with increasing analyte concentration and applied voltage gradient. Linear correlation coefficients are found to over 99.9% for each the curve. Using the best fitting technique, the sensor curve equations are obtained as $\Delta f(GHz) = -(0.02508 + 3.968 \times 10^{-5} \times \nabla\Phi(V/cm)^{2.31}) \times C_1(pM)$

and $\Delta f(GHz) = -(0.02808 + 2.252 \times 10^{-5} \times \nabla\Phi(V/cm)^{2.7}) \times C_1(pM)$

for the first and second orders of WGM, respectively. The correlations show a linear relationship between the concentration and the frequency shift. The frequency shift is also influenced by the applied voltage gradient, in a more significant way, since the external electrical field significantly enhances the adsorption in the controlled applied voltage range, which in turn induces frequency shifts. Moreover, the first order of WGM illustrates a lower order of exponent relationship comparing with the second order of WGM. It means that the applied voltage gradient's effect on the frequency shift is more significant with the second order of WGM since more fraction of the propagating WGM energy overlapped with the more concentrated region, as indicated in Figure 8. This new bio-filtration and sensing system can be utilized for analysis of low-concentration analyte as well as for the study of dynamic adsorption processes.

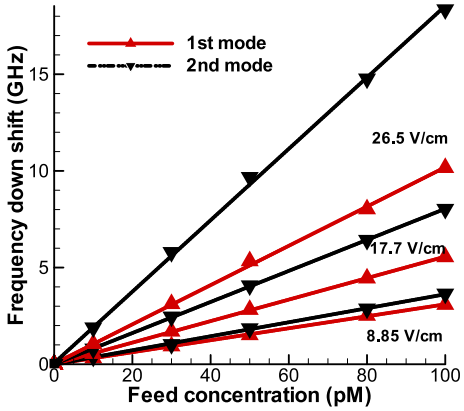

Fig. 10 The sensor curves at steady state versus feed concentrations for cases 8.85 *V/cm*, 17.7 *V/cm*, 26.5 *V/cm* under the first and second order of radial modes resonance.

CONCLUSIONS

The optical WGM micro resonator with integrated functions of the optical sensing and nanofiltration embedded in a microelectrofluidic system is proposed and studied for biological filtration, sensing and chemical analysis for the first time. The analyte is manipulated by an applied external electrical field and directed to the WGM biosensor with a nanoporous structure inside. The analyte solute thus experiences both bulk and nanofiltration flows. The filtration process and analyte concentration are traced by measuring the WGM resonance frequency shift. The whole charged species manipulation and detection processes, including the species transport in the microchannel, adsorption and desorption processes on the pore walls, and the whispering-gallery mode optical resonances, are simulated via the finite element method.

The analyte filtration process varies the effective refractive index of the micro resonator by depositing on pore walls, and thereby can be accurately monitored by tracking the frequency shift over time. The simulated curves fit into the Langmuir-like adsorption kinetics. The time constant for the dynamic adsorption process can be obtained from the frequency shift curve.

A correlation between the frequency shift and the analyte feed concentration and the applied voltage gradient is obtained, revealing a linear relationship between the analyte concentration and the resonance frequency shift and an exponent relationship between the applied voltage gradient and the resonance frequency shift. The applied voltage gradient enhances the shift in an extremely dilute solution. The applied voltage gradient is found to influence the filtration capability through its effect on adsorption and desorption processes. With increasing applied voltage gradient, both the adsorbed analyte surface density on pore walls and the sensor sensitivity increase. The second order of WGM is found to be able to provide a higher sensitivity as compared with the first order.

The WGM sensor is found to function at very low analyte concentrations, down to the pico Molar concentration level.

ACKNOWLEDGMENTS

This material is based upon work supported by a USDA NRI competitive grants program award, 2008-01336.

REFERENCES

[1] P. Eriksson, "Nanofiltration Extends the Range of Membrane Filtration," *Environmental Progress,* **7**, pp. 58-62, 1988.

[2] P. Brandhuber and G. Amy, "Alternative methods for membrane filtration of arsenic from drinking water," *Desalination,* **117**, pp. 1-10, 1998.

[3] D. F. Stamatialis, I. Frenzel, and M. Wessling, "Water recycling from mixed chromic acid waste effluents by membrane technology," *Separation and Purification Technology,* **49**, pp. 76-83, 2006.

[4] W. M. Samhaber, "Uses and problems of nanofiltration in the food industry," *Chemie Ingenieur Technik,* **77**, pp. 583-588, 2005.

[5] A. M. Hassan, M. A. K. Al-Sofi, A. S. Al-Amoudi, A. T. M. Jamaluddin, A. M. Farooque, A. Rowaili, A. G. I. Dalvi, N. M. Kither, G. M. Mustafa, and I. A. R. Al-Tisan, "A new approach to membrane and thermal seawater desalination processes using nanofiltration

membranes (Part 1)," *Desalination,* **118**, pp. 35-51, 1998.

[6] B. Van der Bruggen, E. Curcio, and E. Drioli, "Process intensification in the textile industry: the role of membrane technology," *Journal of Environmental Management,* **73**, pp. 267-274, 2004.

[7] Y. Yoon, P. Westerhoff, S. A. Snyder, E. C. Wert, and J. Yoon, "Removal of endocrine disrupting compounds and pharmaceuticals by nanofiltration and ultrafiltration membranes," *Desalination,* **202**, pp. 16-23, 2007.

[8] X. L. Wang, T. Tsuru, S. Nakao, and S. Kimura, "Electrolyte Transport through Nanofiltration Membranes by the Space-Charge Model and the Comparison with Teorell-Meyer-Sievers Model," *Journal of Membrane Science,* **103**, pp. 117-133, 14 1995.

[9] A. E. Yaroshchuk and Y. A. Vovkogon, "Phenomenological Theory of Pressure-Driven Transport of Ternary Electrolyte-Solutions with a Common Coion and Its Specification for Capillary Space-Charge Model," *Journal of Membrane Science,* **86**, pp. 1-18, 1994.

[10] K. Vafai, Tien, C. L, "Boundary and inertia effects on flow and heat transfer in porous media," *Int. J. Heat Mass Transfer,* **24**, p. 196-203, 1980.

[11] W. R. Bowen and H. Mukhtar, "Characterisation and prediction of separation performance of nanofiltration membranes," *Journal of Membrane Science,* **112**, pp. 263-274, 1996.

[12] W. R. Bowen, A. W. Mohammad, and N. Hilal, "Characterisation of nanofiltration membranes for predictive purposes - Use of salts, uncharged solutes and atomic force microscopy," *Journal of Membrane Science,* **126**, pp. 91-105, 1997.

[13] J. Palmeri, P. Blanc, A. Larbot, and P. David, "Theory of pressure-driven transport of neutral solutes and ions in porous ceramic nanofiltration membranes," *Journal of Membrane Science,* **160**, pp. 141-170, 1999.

[14] P. Fievet, C. Labbez, A. Szymczyk, A. Vidonne, A. Foissy, and J. Pagetti, "Electrolyte transport through amphoteric nanofiltration membranes," *Chemical Engineering Science,* **57**, pp. 2921-2931, 2002.

[15] C. Labbez, P. Fievet, F. Thomas, A. Szymczyk, A. Vidonne, A. Foissy, and P. Pagetti, "Evaluation of the "DSPM" model on a titania membrane: measurements of charged and uncharged solute retention, electrokinetic charge, pore size, and water permeability," *Journal of Colloid and Interface Science,* **262**, pp. 200-211, 2003.

[16] A. Q. Liu, H. J. Huang, L. K. Chin, Y. F. Yu, and X. C. Li, "Label-free detection with micro optical fluidic systems (MOFS): a review," *Analytical and Bioanalytical Chemistry,* **391**, pp. 2443-2452, 2008.

[17] Z. Guo, S. Maruyama, and A. Komiya, "Rapid yet accurate measurement of mass diffusion coefficients by phase shifting interferometer," *Journal of Physics D-Applied Physics,* **32**, pp. 995-999, 1999.

[18] A. J. deMello, S. A. Leung, R. F. Winkle, and R. C. R. Wootton, "A method for rapid reaction optimisation in continuous-flow microfluidic reactors using online Raman spectroscopic detection," *Analyst,* **130**, pp. 46-51, 2005.

[19] X. Q. Cui, X. Heng, J. G. Wu, Z. Yaqoob, A. Scherer, D. Psaltis, and C. H. Yang, "Slanted hole array beam profiler (SHArP)- a high-resolution portable beam profiler based on a linear aperture array," *Optics Letters,* **31**, pp. 3161-3163, 2006.

[20] S. R. Manalis, S. Son, W. H. Grover, and T. P. Burg, "Suspended microchannel resonators for ultralow volume universal detection," *Analytical Chemistry,* **80**, pp. 4757-4760, 2008.

[21] A. Q. Liu, Y. Sun, C. S. Lim, T. C. Ayi, and P. H. Yap, "Design, simulation and experiment of electroosmotic microfluidic chip for cell sorting," *Sensors and Actuators a-Physical,* **133**, pp. 340-348, 2007.

[22] H. Quan and Z. Guo, "Simulation of single transparent molecule interaction with an optical microcavity," *Nanotechnology,* **18**, 375702, 2007.

[23] S. Arnold, M. Khoshsima, I. Teraoka, S. Holler, and F. Vollmer, "Shift of whispering-gallery modes in microspheres by protein adsorption," *Optics Letters,* **28**, pp. 272-274, 2003.

[24] H. Quan and Z. Guo, "Simulation of whispering-gallery-mode resonance shifts for optical miniature biosensors," *Journal of Quantitative Spectroscopy & Radiative Transfer,* **93**, pp. 231-243, 2005.

[25] S. Arnold and F. Vollmer, "Whispering-gallery-mode biosensing: label-free detection down to single molecules," *Nature Methods,* **5**, pp. 591-596, 2008.

[26] P. Kowalski, I. Oledzka, P. Okoniewski, M. Switala, and H. Lamparczyk, "Determination of streptomycin in eggs yolk by capillary electrophoresis," *Chromatographia,* **50**, pp. 101-104, 1999.

[27] Available: http://www.chemspider.com/

[28] S. Mezzasalma and D. Baldovino, "Characterization of silicon nitride surface in water and acid environment: A general approach to the colloidal suspensions," *Journal of Colloid and Interface Science,* **180**, pp. 413-420, 1996.

[29] N. H. Cheung, K. M. Yeung, and Z. J. Lu, "Adsorption of bovine serum albumin on fused silica: Elucidation of protein-protein interactions by single-molecule fluorescence microscopy," *Colloids and Surfaces B-Biointerfaces,* **69**, pp. 246-250, 2009.

[30] B. H. Crichto, Li, H., Fouracre, R. A., "The effect of hydrogen ions in electrolytic solutions on water tree growth in LDPE," in *Sixth Int. Conference on Dielectric materials, Measurements and Applications*, Manchester, UK, 7-10 September,1992.

[31] E. Samson, J. Marchand, and K. A. Snyder, "Calculation of ionic diffusion coefficients on the basis of migration test results," *Materials and Structures,* **36**, pp. 156-165, 2003.

[32] H. Lin, B. D. Storey, M. H. Oddy, C. H. Chen, and J. G. Santiago, "Instability of electrokinetic microchannel flows with conductivity gradients," *Physics of Fluids,* **16**, pp. 1922-1935, 2004.

[33] B. C. Shi, Z. H. Chai, and Z. L. Guo, "Study of electro-osmotic flows in microchannels packed with variable porosity media via lattice Boltzmann method," *Journal of Applied Physics,* **101**, 104913, 2007.

[34] J. D. Jackson, *Classical Electrodynamics*. New York: Wiley, 1998.

[35] J. Lu, Siu, T. J., Howlin, B. J., Thomas, R. K., Cui, Z., Penfold, J., Webster, J. R. P., "Protein-adsorption at interfaces," *Scientific Highlights,* **1**, p. 2, 1998.

[36] A. B. Michelle, Tie, Y. R., Paul, R. V. T., "Protein adsorption kinetics under an applied electric field: An optical waveguide lightmode spectroscopy study," *Langmuir,* **19**, p. 9, 2003.

[37] L. Huang and Z. Guo, "Biosensing in a microelectrofluidic system using optical whispering-gallery mode spectroscopy," *Biomicrofluidics,* **5**, 034114, 2011.

[38] N. H. Cheung, K. C. Kwok, and K. M. Yeung, "Adsorption kinetics of bovine serum albumin on fused silica: Population heterogeneities revealed by single-molecule fluorescence microscopy," *Langmuir,* **23**, pp. 1948-1952, 2007.